A. Zare[1,2]
School of Mechanical and Aerospace Engineering,
Oklahoma State University,
Stillwater, OK 74078
e-mail: azare1@jhu.edu

M. Tunesi
School of Mechanical and Aerospace Engineering,
Oklahoma State University,
Stillwater, OK 74078
e-mail: michele.tunesi@okstate.edu

T. A. Harriman
School of Mechanical and Aerospace Engineering,
Oklahoma State University,
Stillwater, OK 74078
e-mail: tres.harriman@okstate.edu

J. R. Troutman
Center for Precision Metrology,
University of North Carolina at Charlotte,
Charlotte, NC 28223
e-mail: jtleafs33@gmail.com

M. A. Davies[3]
Center for Precision Metrology,
University of North Carolina at Charlotte,
Charlotte, NC 28223
e-mail: matt.davies@nanotechsys.com

D. A. Lucca
School of Mechanical and Aerospace Engineering,
Oklahoma State University,
Stillwater, OK 74078
e-mail: lucca@okstate.edu

Face Turning of Single Crystal (111)Ge: Cutting Mechanics and Surface/Subsurface Characteristics

Single crystal Ge is a semiconductor that has broad applications, especially in manipulation of infrared light. Diamond machining enables the efficient production of surfaces with tolerances required by the optical industry. During machining of anisotropic single crystals, the cutting direction with respect to the in-plane lattice orientation plays a fundamental role in the final quality of the surface and subsurface. In this study, on-axis face turning experiments were performed on an undoped (111)Ge wafer to investigate the effects of crystal anisotropy and feedrate on the surface and subsurface conditions. Atomic force microscopy and scanning white light interferometry were used to characterize the presence of brittle fracture on the machined surfaces and to evaluate the resultant surface roughness. Raman spectroscopy was performed to evaluate the residual stresses and lattice disorder induced by the tool during machining. Nanoindentation with Berkovich and cube corner indenter tips was performed to evaluate elastic modulus, hardness, and fracture toughness of the machined surfaces and to study their variations with feedrate and cutting direction. Post-indentation studies of selected indentations were also performed to characterize the corresponding quasi-plasticity mechanisms. It was found that an increase of feedrate produced a rotation of the resultant force imparted by the tool indicating a shift from indentation-dominant to cutting-dominant behavior. Fracture increased with the feedrate and showed a higher propensity when the cutting direction belonged to the $<11\bar{2}>$ *family.* [DOI: 10.1115/1.4057054]

Keywords: brittle fracture anisotropy, diamond turning, dislocation pinning, indentation pop-in, indentation elbow, machining processes, precision and ultra-precision machining

1 Introduction

Infrared (IR)-transparent materials are used in the production of optical elements, with applications that can range from thermal sensors to imaging systems. One of the materials commonly used in such devices is single crystal Ge [1], for its transmittance in the spectral range from 2 μm up to 14 μm [2]. Bulk single crystals of Ge can be produced by the Czochralski method, with excellent crystal quality and accurate orientation. The single crystal can then be machined by single-point diamond turning, in which a stationary tool is fed across a rotating workpiece, to obtain a rotationally symmetric optical element that has the required tolerances for surface roughness and form accuracy. Turning is also commonly used to establish a planar surface perpendicular to the main spindle axis prior to more complex cutting geometries, such as fly-cutting [3,4].

Single crystal Ge is prone to undergo brittle fracture when machined. One of the important factors that determine the onset of fracture on the surface is the relationship between the crystallographic orientation of the specimen and the cutting direction of the tool. The anisotropic response to machining of single crystal Ge was first studied by Nakasuji et al. by performing on-axis turning experiments, and therefore cutting the surface with all possible in-plane cutting directions [5]. It was found that the surface condition was dependent on the relationship between the cutting direction and the lattice symmetry. Some cutting directions resulted in brittle fracture on the surface while others produced an apparent fracture-free surface. In our previous studies on the subsurface damage produced by single point diamond turning of single crystal Ge [4,6], ion channeling and Raman spectroscopy were employed and showed that there was an increase in lattice disorder in the near subsurface as the feedrate increased. There was also a change in the spatial distribution of the lattice disorder, which reached deeper below the surface for larger feedrates. In addition to surface and subsurface damage, diamond turning has been shown to introduce residual stresses into the machined surface with the magnitude and state of stress varying as a function of distance below the surface [3,7,8].

For machined components, characterization of the surface and subsurface damage is an important consideration because it affects both the optical and mechanical properties and therefore dictates the functional performance and lifetime of the optical elements [9–11]. Considering that surface roughness, lattice order below the surface, and machining-induced residual stresses all depend on the cutting parameters, it is important to assess the material condition after the new surface is generated. In this study, the combined effects of crystal anisotropy and feedrate were investigated by machining undoped single crystal specimens of (111)Ge using on-axis face turning with a single crystal diamond tool. The forces were measured during cutting. The machined surfaces were then characterized by several techniques. Nanoindentation was

[1]Corresponding author.
[2]Present address: Department of Mechanical Engineering, Johns Hopkins University, Baltimore, MD 21218.
[3]Present address: Moore Nanotechnology Systems, Charlotte, NC 28216.
Manuscript received November 17, 2022; final manuscript received February 27, 2023; published online March 28, 2023. Assoc. Editor: Vincent Wagner.

used to determine the elastic and plastic response of the surface, as well as to evaluate the fracture toughness of the material. Atomic force microscopy (AFM), scanning white light interferometry (SWLI), and Raman spectroscopy were used to characterize the surface topography and the crystalline quality of the lattice immediately below the surface. AFM and scanning electron microscopy (SEM) were also used to image the residual impressions left by the indenter.

2 Experimental Details

2.1 Preparation of Surfaces. An undoped single crystal (111) Ge wafer with a diameter of 25 mm and a thickness of 1 mm was obtained from Novotech, Inc (Action MA, USA). The as-received wafer was chemomechanically polished to an average surface roughness (Ra) of ~2.2 nm. The wafer was mounted on a custom vacuum chuck and face turned on-axis using a Moore 350 Freeform Generator ultra-precision diamond machining center (see Fig. 1(*a*)) which had a linear and rotational resolution of 0.01 nm and 0.1 μ°, respectively. The cutting experiments were performed using a round nose single crystal diamond tool (see Fig. 1(*b*)) with a nose radius (R) of 1 mm and a rake angle of −25 deg. The spindle speed per revolution was adjusted for each band such that a cutting speed (V_c) of 4 m/s was obtained at the center of each band. Because of the relatively small change in radius within each band compared to the distance from the center of the spindle, the cutting speed for each band varied no more than ±6% from 4 m/s. The nominal depth of cut (t_c) was also held constant at 5 μm. The feedrate was varied (f = 0.5, 1, 2, 3, 5, 7, and 9 μm/rev) to create a total of seven concentric bands each with a width of ~1 mm on the workpiece surface. Figure 1(*c*) shows the turned surfaces, where a shaded tri-lobed pattern corresponding to regions of increased surface roughness associated with brittle fracture is marked in red. As detailed in our previous study and those of others [4,5], in face turning of a (111)Ge single crystal, increased fracture is observed when cutting along the [1$\bar{2}$1], [11$\bar{2}$], or [$\bar{2}$11] in-plane orientations. Regions in between these lobes, centered along the [2$\bar{1}\bar{1}$], [$\bar{1}$2$\bar{1}$], or [$\bar{1}\bar{1}$2] in-plane orientations, have a lower propensity for fracture and therefore exhibit a lower overall surface roughness. A model of single crystal Ge with those cutting directions highlighted is presented in Fig. 2. Experiments performed at the center of the lobes with increased fracture had the cutting direction belonging to the <11$\bar{2}$> family, while experiments performed in between the lobes had the cutting direction belonging to the <2$\bar{1}\bar{1}$> family.

The force exerted by the tool was recorded during the cutting experiments by mounting the tool on top of a Kistler 9256C1

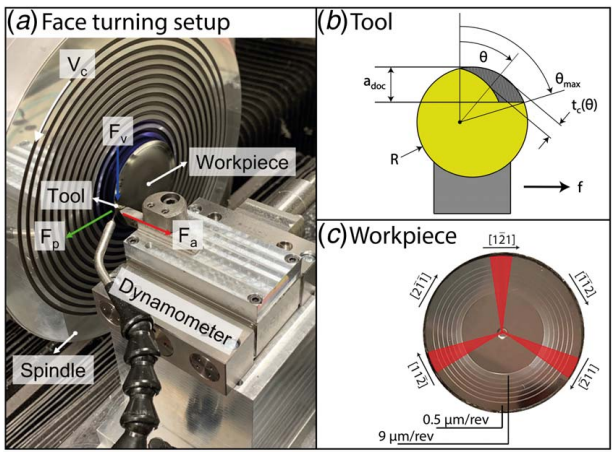

Fig. 1 Schematic representation of the (*a*) face turning geometry and force components, (*b*) cutting tool, and (*c*) the (111)Ge turned surfaces with the regions of increased brittle fracture along the <11$\bar{2}$> cutting directions marked by highlights

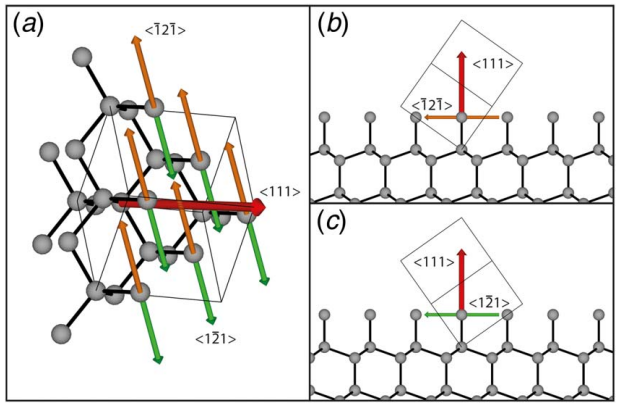

Fig. 2 Sections of the diamond cubic lattice structure produced with VESTA software [12]: (*a*) a lattice unit delimited by the (111) plane, (*b*) – (c) section of a (111) Ge plane with respect to each cutting direction

miniature dynamometer comprised of a fluid-proof piezoelectric. The range and resolution of the dynamometer were ±250 N and 0.002 N, respectively. The unloaded natural frequency of the dynamometer (~5 kHz) was reduced by nearly 40% (~3 kHz) upon loading it with the tool assembly. Thus, inverse filtering was applied to extend the usable frequency range beyond the reduced natural limit. A Kistler type 5010 dual mode charge amplifier was then used to convert the charge output to voltage.

2.2 Evaluation of Surface/Subsurface Characteristics. Surface topography of the turned surfaces along the <11$\bar{2}$> and <2$\bar{1}\bar{1}$> cutting directions was characterized using a commercial atomic force microscope. The AFM scans were collected using tapping mode. Quantitative values of areal surface roughness (Sa) were also obtained using a Zygo Newview 5000 scanning white light interferometer.

Near-surface lattice disorder along the <11$\bar{2}$> and <2$\bar{1}\bar{1}$> cutting directions was studied by Raman spectroscopy using a confocal microscope in a backscattering configuration. Light with a wavelength of 532 nm was directed at an incident angle normal to the surface through a 100x/0.9NA objective. The same objective was used to collect the scattered light in reflection. The collected light was then focused onto a 50 μm diameter optical fiber which acted as a confocal pinhole. A 0.3 m monochromator with an 1800 groove/mm grating was subsequently used to disperse the light. Finally, a thermoelectrically cooled charge coupled device (CCD) camera was used to detect the light. The excitation spot was scanned over the area of interest using a piezoelectrically driven stage. Each collected spectrum was fitted to a Lorentzian curve using the microscope software to quantify the spatial variations in the Raman response. Spatial maps of the Raman peak intensity, spectral center, and width were then created based on the curve fitting results. Histograms of the spectral center and peak width were subsequently generated using the obtained spatial maps. To avoid anomalous features in the spectra (e.g., cosmic rays), the highest and lowest 1% of the histogram population were omitted in the calculation of the average and standard deviation. The laser power was optimized to minimize heating of the specimen while producing a peak intensity of the spectra to allow for Lorentzian curve fitting.

Mechanical response of the turned surfaces was studied by nanoindentation experiments performed with a Hysitron Triboindenter in load controlled mode. The specimen was left inside the instrument chamber overnight to allow for thermal equilibration. Furthermore, the instrument's drift rate was monitored over a 5 s interval in the beginning of each indentation and results were excluded when the drift was higher than 0.1 nm/s. The system was calibrated by calculating the area function of the indenter and

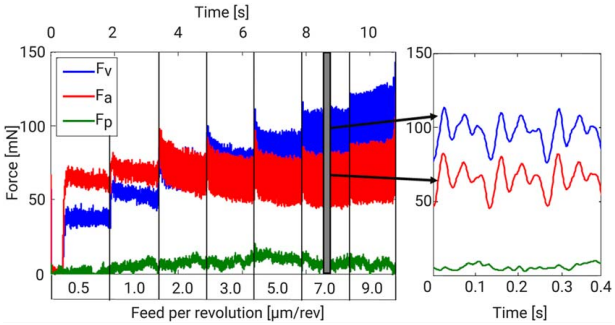

Fig. 3 Representative measured cutting forces during face turning of the (111)Ge for a range of feedrates. Details of one region are shown on right where fluctuations in the force correspond to the cutting tool entering and exiting the regions where brittle fracture increases.

the instrument's frame compliance by performing indentations in fused silica and tungsten reference specimens using the procedure of Oliver and Pharr [13] and of ISO 14577 [14]. A diamond Berkovich indenter was used to measure elastic modulus and hardness of the turned surfaces along both the $<11\bar{2}>$ and $<2\bar{1}\bar{1}>$ cutting directions. In addition, a diamond cube corner indenter was used to study the effects of feedrate on indentation fracture toughness of the turned surfaces along the $<11\bar{2}>$ cutting direction. For both the Berkovich and cube corner indentations, the load applied to the indenter was increased over a 30 s interval to the selected maximum force followed by a 60 s hold to minimize any time-dependent plastic deformation. Then, the load was decreased to 10% of the maximum applied force over a 10 s interval followed by another 60 s hold to evaluate and compensate for the remaining thermal drift. Finally, the indenter was fully unloaded over a 2 s interval. The AFM was used to examine the areas around selected Berkovich indentations to characterize the deformation mechanisms. The indentations made with the cube corner indenter were studied by a Hitachi S-4800 field emission scanning electron microscope to measure the length of the radial cracks formed as a result of indentation. The obtained crack lengths were then used to evaluate the indentation fracture toughness of the turned surfaces.

3 Results and Discussion

3.1 Cutting Forces. Figure 3 shows the three force components measured during turning at different feedrates after filtering the raw data using a low-pass third-order Butterworth filter with a cutoff frequency of 500 Hz. A crossover of F_v and F_a is observed at $1 < f < 3$ μm/rev, indicating a shift from indentation-dominant to cutting-dominant behavior. A closer examination of the forces, sampled in the inset of Fig. 3, shows three force oscillations during each revolution. These oscillations are caused by the in-plane anisotropy of brittle fracture in (111)Ge as the force magnitude decreases when cutting along the $<11\bar{2}>$ directions. The cutting directions along which brittle fracture occurs are marked in red in Fig. 1(*c*). At all feedrates, F_p is much smaller than the other two force components, as expected. The average values of the three force components along with the peak-to-valley range of oscillations are shown in Fig. 4(*a*). Increasing the feedrate from 0.5 μm/rev to 9 μm/rev resulted in a monotonic increase in the cutting force F_v from 35 mN to 105 mN, while F_a varied nonmonotonically between the values of 50 mN and 63 mN. The maximum chip thickness, shown on the top axis of Fig. 4(*a*), was estimated geometrically by calculating θ_{max} in Fig. 1(*b*). For all feedrates, θ_{max} was between 5.7 deg and 6.0 deg. The maximum chip thickness was then computed using:

$$t_{max} = f \sin \theta_{max} \tag{1}$$

As shown in Fig. 4(*b*), the relative increase of F_v compared to F_a resulted in the rotation of the resultant force angle (δ) from 56 deg at $f = 0.5$ μm/rev to 31 deg at $f = 9$ μm/rev. This indicates a transition from indentation-dominant to cutting-dominant behavior at higher feedrates and is consistent with our previous observations from round-nosed flycutting of (111)Ge over a range of feedrates [4].

3.2 Surface/Subsurface Characteristics. Figure 5 shows 50×50 μm^2 AFM scans of surfaces turned along the $<11\bar{2}>$ and $<2\bar{1}\bar{1}>$ cutting directions. In general, surfaces machined with $f < 3$ μm/rev show limited amount of fracture as demonstrated by the lack of pits. At $f = 3$ μm/rev, surface pits began to appear, visualized as ellipsoids with dark rims and bright centers. The emergence of surface pits was accompanied by ~4 nm and ~300 nm jumps in the average surface roughness (Ra) and average maximum roughness height (R_{max}), respectively. The number, area, and depth of the pits monotonically increased at larger feedrates. Surfaces turned along the $<2\bar{1}\bar{1}>$ cutting directions that had evidence of surface fracture show fewer number of pits with larger areal sizes compared to the surfaces created along the $<11\bar{2}>$ cutting directions. To provide a quantitative comparison between the surface roughness values along the $<11\bar{2}>$ and $<2\bar{1}\bar{1}>$ cutting directions, variations in surface roughness were also studied by SWLI over a

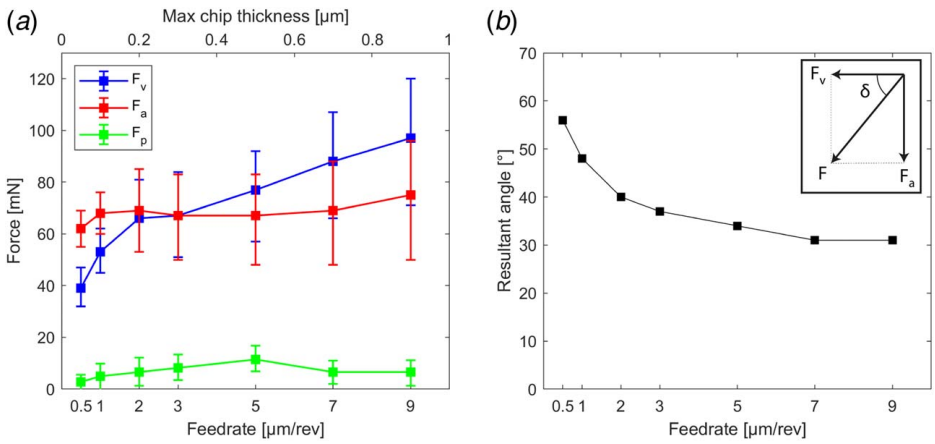

Fig. 4 (*a*) Measured average forces during face turning of (111)Ge as a function of feedrate and maximum chip thickness. The error bars represent the maximum and minimum force for a full turn of the specimen and (*b*) resultant force angle calculated from the average value of the thrust and cutting forces.

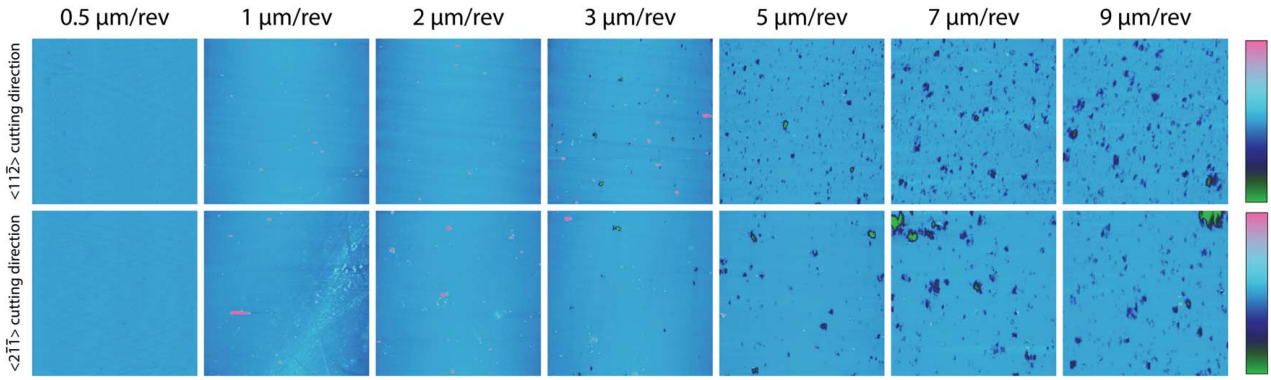

Fig. 5 Top view surface topography of the (111)Ge surfaces turned with a range of feedrates along the <11$\bar{2}$> and <2$\bar{1}\bar{1}$> cutting directions. The scan area is 50 × 50 μm^2 for all feedrates. The height scale is 50 nm for $f = 0.5$ μm/rev, 100 nm for $f = 1$, 2, and 3 μm/rev, 500 nm for $f = 5$ μm/rev, 700 m for $f = 7$ μm/rev, and 1000 nm for $f = 9$ μm/rev.

408×408 μm^2 area. For each family of cutting directions, three separate areas were scanned at each feedrate to obtain the average Sa values and corresponding standard deviations reported in Fig. 6. Increasing the feedrate led to an initial decrease in Sa for $f < 3$ μm/rev, followed by an increase at higher feedrates. This is consistent with the AFM observations that only showed evidence of brittle surface fracture at $f \geq 3$ μm/rev. After the onset of brittle surface fracture, the average Sa of the surfaces turned along the <2$\bar{1}\bar{1}$> cutting directions are consistently lower than those along the <11$\bar{2}$> cutting directions. This agrees with the observed force oscillations during each revolution (shown in the inset of Fig. 3) suggesting a higher propensity for brittle fracture along the <11$\bar{2}$> cutting directions.

The subsurface damage of the turned surfaces was investigated by Raman spectroscopy. Spatial mapping of the Raman response was performed on 25×25 μm^2 areas with 676 individual spectra being collected from each scanned area. A typical Raman spectrum of the surface turned with $f = 0.5$ μm/rev along the <11$\bar{2}$> cutting direction is shown in Fig. 7. The spectrum shows only one peak centered at ~300.6 cm^{-1} which has been attributed to the triply degenerate crystalline Ge mode. The Ge Raman peak was fit with a Lorentzian peak shape, and histograms of the results were used to determine the peak width (FWHM) and peak center. The FWHM of the Raman peak has been correlated with the crystalline quality of semiconductors (Ge, Si, and GaAs) where lattice disorder decreases the phonon lifetime and thus results in peak broadening. Therefore, variations in the FWHM can be used to qualitatively distinguish between regions of different crystal quality [15–19]. Figure 8(*a*) shows the average and standard deviation of the FWHM for the turned surfaces along both families of cutting directions. Increasing the feedrate results in an overall increase in the FWHM of the Raman mode from 6.7 ± 0.3 cm^{-1} to 10.3 ± 1.5 cm^{-1}, indicating an increase in lattice disorder below the surface. Furthermore, Fig. 8(*a*) shows larger standard deviations of the FWHM at $f \geq 3$ μm/rev as evidenced by the larger error bars. This shows that the FWHM varies more over the set of points collected on the surface, therefore suggesting an increase in the spatial variations of the subsurface damage. The damage is also seen to be higher for the surfaces cut along the <11$\bar{2}$> cutting directions further supporting the in-plane anisotropy of brittle fracture in (111)Ge.

The average and standard deviation of the Raman peak center were measured for surfaces turned with different feedrates along both families of cutting directions. Increasing the feedrate was seen to result in a shift of the peak center to higher wavenumbers, indicating a more compressive residual stress [8]. Residual stress

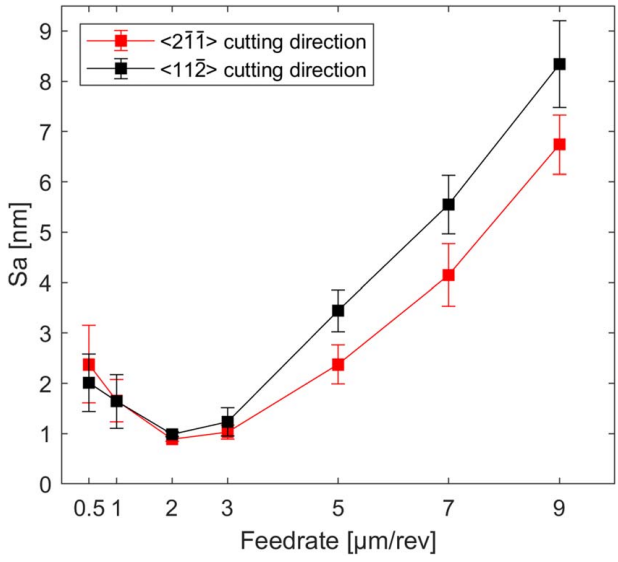

Fig. 6 Areal surface roughness (Sa) of the (111)Ge surfaces turned with a range of feedrates along the <11$\bar{2}$> and <2$\bar{1}\bar{1}$> cutting directions

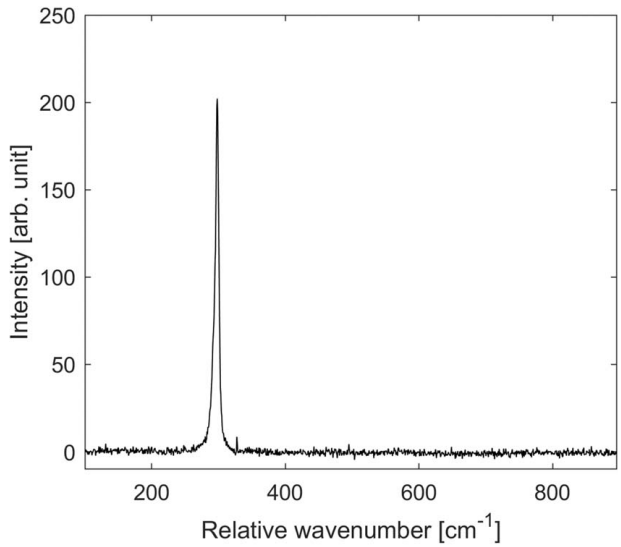

Fig. 7 A typical Raman spectrum of the (111)Ge surface turned with $f = 0.5$ μm/rev along the <11$\bar{2}$> cutting directions

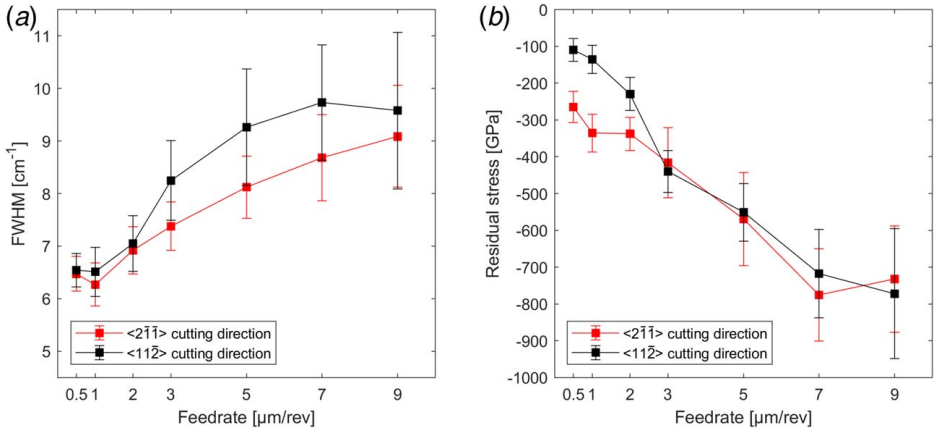

Fig. 8 Average and standard deviation of (*a*) the Raman mode FWHM and (*b*) residual stress measured from the shifts in Raman mode peak position for the (111)Ge surfaces turned with a range of feedrates along the <11$\bar{2}$> and <2$\bar{1}\bar{1}$> cutting directions

is generated below the surface whenever inhomogeneous deformation occurs [20]. When cutting-induced thermal effects are negligible, the residual stress below the surface is typically compressive [21]. Previous reports of the effects of applied hydrostatic pressure on the position of the Ge Raman mode allow for the residual stress to be estimated using $\sigma = 260(300.6 - \omega)$, where σ is the stress in MPa and ω is the measured center of the crystalline Ge Raman mode (the stress-free center is 300.6 cm^{-1}) [22,23]. The values of residual stress estimated from the shifts in Raman mode peak position are shown in Fig. 8(*b*). In general, increasing the feedrate resulted in higher magnitudes of compressive residual stress and larger standard deviations along both the <11$\bar{2}$> and <2$\bar{1}\bar{1}$> cutting directions. Prior to the onset of brittle surface fracture ($f <$ 3 μm/rev), the magnitude of the compressive residual stress along the <2$\bar{1}\bar{1}$> cutting directions was found to be larger than that along the <11$\bar{2}$> cutting directions. It is speculated that the material machined along the <11$\bar{2}$> cutting directions relieved some of the compressive stress generated by the tool through fracture. Fracturing allows the lattice to reorganize and liberate some of the stress while maintaining the crystallinity. For $f \geq 3$, there was no clear difference in residual stress when comparing the two machining direction families, likely due to the pronounced fracture below the surface.

A Berkovich indenter was used to perform nanoindentation experiments on the turned surfaces in order to characterize their mechanical response. Figure 9 shows representative curves of the applied indentation force (P) plotted against penetration depth (h) for the surfaces turned with the lowest (0.5 μm/rev) and highest (9 μm/rev) feedrates along both families of cutting directions. Each curve shows loading, hold at a maximum force (P_{max}) of 10 mN, and unloading. Multiple small pop-ins can also be observed in the loading portion of the curves. Indentation pop-ins of single crystal Ge have been attributed to a variety of instability mechanisms including phase transformation from a diamond cubic to a denser metallic phase (β-Sn) during loading [24], discontinuous crack extension and chipping [25], and deformation via slip/defect propagation [24,26]. To identify the mechanism contributing to the pop-ins observed in the present study, a series of Berkovich indentations were performed on the surface turned with $f = 1$ μm/rev along the <11$\bar{2}$> cutting directions. These indentations were performed over a range of maximum forces ($P_{max} = 1$, 2, 3, 4, 5, 6, 8, or 10 mN) and the residual impressions were studied by AFM. Figures 10 and 11 show the force versus penetration depth curves and the corresponding post-indentation AFM images obtained at P_{max} of 5 mN and 6 mN. For the maximum applied force of 5 mN, the loading portion of the force versus penetration depth curves is seen to be smooth and no cracks are observed in the corresponding AFM images. Similar observations were made when indentations were performed at $P_{max} < 5$ mN. Increasing the maximum applied force to 6 mN, however, results in formation of pop-ins in the force versus penetration depth curve. Furthermore, radial cracks are found to emanate from the corners of the corresponding residual impressions. It is thus concluded that the pop-ins observed in the force versus penetration depth curves of Berkovich indentations are resultant from the formation or extension of radial cracks.

Reduced elastic modulus (E_r) and hardness (H) of the turned surfaces were obtained using the method of Oliver and Pharr [13] by fitting a power law function to the unloading curve, excluding the last portion of the data. The function $P(h)$ was then used to calculate the contact stiffness ($S = dP/dh$) and the area of contact (A) at P_{max}. Values of E_r and H were then obtained using

$$E_r = \frac{\sqrt{\pi}}{2}\frac{S}{\sqrt{A}} \tag{2}$$

$$H = \frac{P_{max}}{A} \tag{3}$$

The obtained values of E_r were converted to elastic modulus (E) to account for the indenter's elasticity

$$E = (1 - \nu^2)\left[\frac{1}{E_r} - \frac{1 - \nu_i^2}{E_i}\right]^{-1} \tag{4}$$

where ν is the Poisson's ratio for the specimen (0.21 for Ge [27,28]) and E_i and ν_i represent the elastic modulus and Poisson's ratio for the diamond indenter (1141 GPa and 0.07, respectively [29]). It is noted that formation of radial cracks at $P_{max} \geq 6$ mN (discussed previously in Figs. 10 and 11) did not result in any noticeable changes in the modulus and hardness. Therefore, the mechanical response of the turned surfaces was compared by performing at least six indentations at a P_{max} of 10 mN. Figure 12 shows the obtained average values of E, S, and H along with one standard deviation. For the surface turned with $f = 0.5$ μm/rev along the <2$\bar{1}\bar{1}$> cutting direction, an elastic modulus of 138.3 GPa and a hardness of 11.4 GPa were obtained. Increasing the feedrate resulted in an overall increase in the elastic modulus, as shown in Fig. 12(*a*), with higher values obtained along the <11$\bar{2}$> cutting directions. Since elastic modulus is an intrinsic property of the material, a monotonic increase can indicate either bias in the computation method or a change on the atomic scale of the lattice. Considering Eq. (3), both contact area and stiffness can affect the computed modulus. Tsui et al. [30] showed that during nanoindentation on specimens pre-stressed with an imposed compressive load, the contact area tends to be underestimated due to the occurrence of pile-up in the

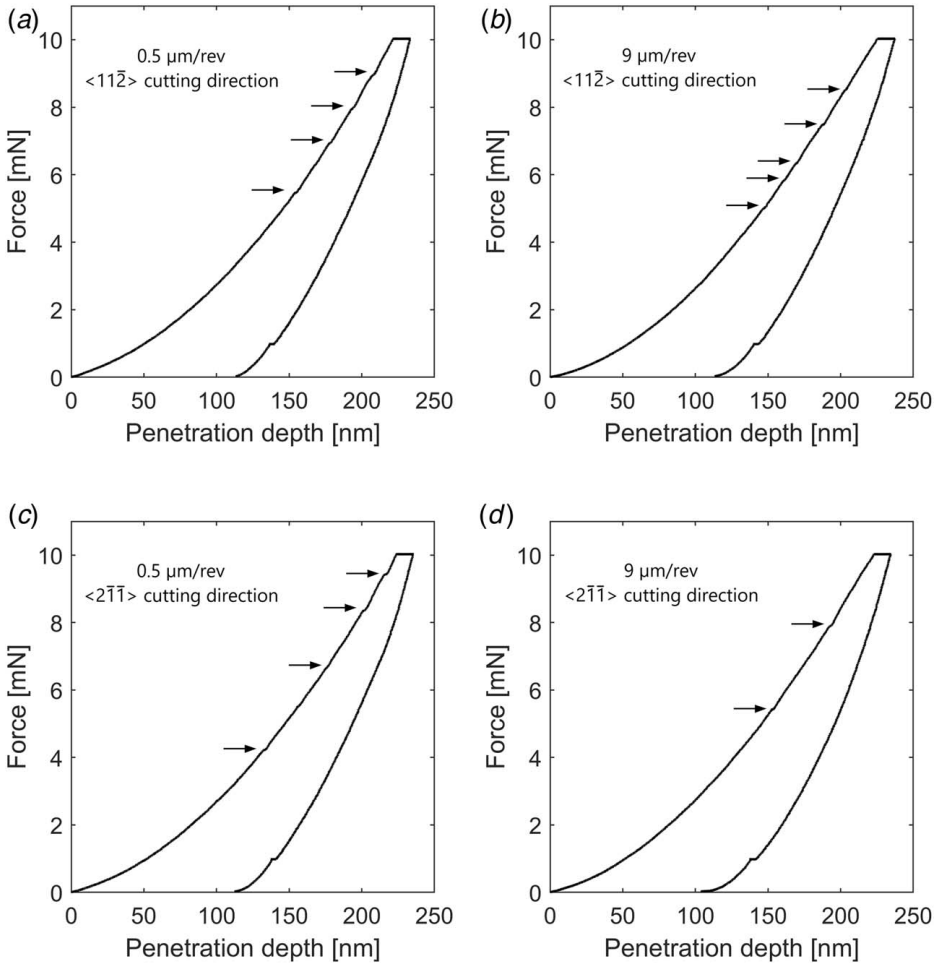

Fig. 9 Force applied to the Berkovich indenter plotted against penetration depth for the surfaces turned with a feedrate of (*a*), (*c*) 0.5 μm/rev and (*b*), (*d*) 9 μm/rev. Arrows denote the observed pop-ins.

region immediately outside the contact region of the indenter. However, the method of Oliver and Pharr used for the analysis of nanoindentation data does not take pile-up into consideration. To rule out any error from the computed contact areas, variations of contact stiffness with feedrate were considered instead of modulus. As shown in Fig. 12(*b*), contact stiffness also showed a nearly monotonic increase with feedrate along both families of cutting directions. Considering that the internal state of stress is not expected to affect the measured stiffness [30], the observed increase indicates a change in the elastic interactions at the atomic scale. One possible explanation for the increase in elastic modulus is the progressive pinning of dislocations on defects below the surface. Bauer and Gordon [31] measured an increase of the elastic modulus in alkali halides after X-ray irradiation. X-rays are known to dislocate ions in alkali halides, generating defects like F-centers. In their analysis, the irradiation dose correlated with the increase of the elastic modulus. In another study by Dieckamp and Sosin [32], neutron bombardment was used to generate lattice disorder in Cu, and small amount of irradiation caused the elastic modulus to increase. In both cases the change in elastic modulus was interpreted by considering that dislocations are more likely to be pinned to defect centers with increased lattice disorder, and the more frequent elastic interaction of the pinned dislocations and the defects provides the increase of the elastic modulus. A study on self-implanted single crystal Ge also reported that for an implantation dose of 3×10^{12} ions/cm^2 the elastic modulus increased with respect to the non-implanted specimen [33]. Based on the literature, the following mechanism for dislocation pinning in Ge is proposed. During the loading phase of the indentation, dislocations are nucleated, generally in the first tens of nanometers, and forced to move deeper in the material. If the material was a defect-free single crystal, the only barrier to dislocation movement would be the energy required to cause slip, which has been shown to be a primary carrier of quasi-plasticity in Ge [24,26]. With increasing lattice disorder however, defects could impede the dislocation movement by pinning them. In this case, the dislocations can move through or around the defects, but when the maximum indentation load is reached, they are elastically compressed against the defects. Without the possibility of moving further and with several points locked by the defects, a portion of load is elastically stored in the dislocations that are bowed in between the pinned points. Upon removal of the load, the stored energy is released by the dislocations restoring their original shape and therefore causing the overall stiffness of the material to appear larger. This proposed mechanism is supported by the following observation. The increase of elastic modulus and stiffness agrees with the increase of the FWHM of the Raman mode shown in Fig. 7(*a*) which suggested an increase in lattice disorder at higher feedrates. The relative comparison between the two families of cutting directions also is consistent, with the surfaces turned along the <11$\bar{2}$> cutting directions having a higher value of FWHM and stiffness compared to those along the <2$\bar{1}\bar{1}$> cutting directions. Increased lattice disorder provides more pinning sites and results in a higher elastic modulus. Considering Fig. 12(*c*), increasing the feedrate had little or no effect on hardness. Compressive residual stress is reported to reduce the magnitude of shear stress induced by the

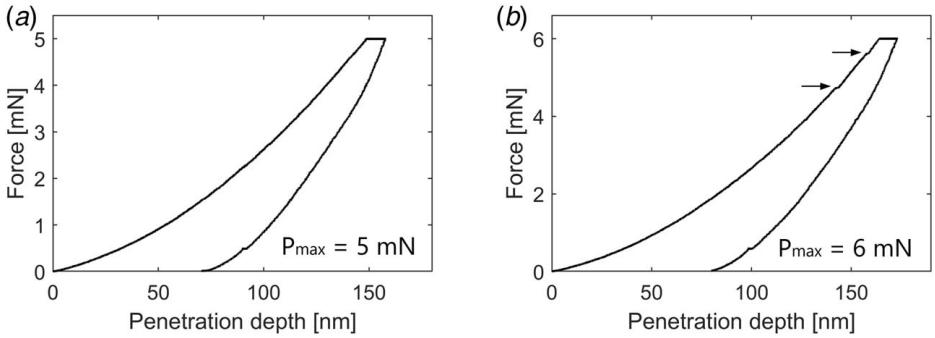

Fig. 10 Force applied to the Berkovich indenter plotted against penetration depth for the surfaces turned with a feedrate of 1 μm/rev along the <11$\bar{2}$> cutting directions. The indentations were performed at a maximum force of (*a*) 5 mN and (*b*) 6 mN. Arrows denote the observed pop-ins.

indenter (relative to a stress-free specimen) and therefore produce smaller residual impressions which result in higher hardness values [34–36]. However, the maximum depths probed by the Berkovich indenter in the present study (230–250 nm) were considerably larger than the probing depth of the Raman excitation light (~10 nm [3]). Therefore, the hardness values are not expected to be altered by the residual compressive stress present in the near-surface region [37]. It is also noted that within the uncertainty of our measurements, no significant anisotropy in hardness is observed between the surfaces turned along the two families of cutting directions at a given feedrate.

The length of radial cracks can be used to evaluate indentation fracture toughness. Although cracks were observed in post-indentation AFM images of Berkovich impressions, precise measurement of the crack lengths was challenging because most cracks were smaller than 400 nm. To accentuate the cracks, another set of nanoindentation experiments was performed using a diamond cube corner indenter. Even though the cube corner and Berkovich indenters both have a tetrahedron geometry, the cube corner indenter is more acute than the Berkovich (centerline-to-face angle of 35.3 deg versus 65.3 deg). Thus, at a given applied force the cube corner indenter displaces a larger volume of material compared to the Berkovich indenter (≥3 times). Subsequently, the applied stresses beneath the cube corner indenter are also greater in magnitude [38]

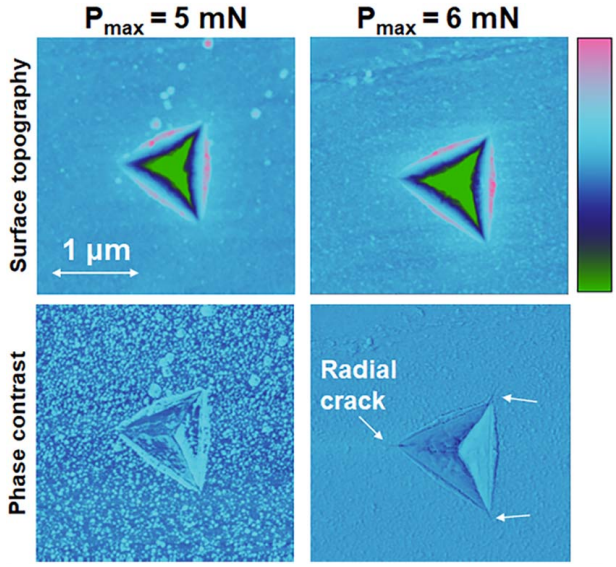

Fig. 11 Post-indentation top view AFM scans of the Berkovich residual impressions on the surfaces turned with a feedrate of 1 μm/rev along the <11$\bar{2}$> cutting directions. The height scale of the surface topography image is 50 nm.

and larger cracks could be generated. Using a cube corner indenter could also result in a phase transformation in Ge from diamond cubic to metallic (β-Sn) phase because the formation and propagation of quasi-plasticity mechanisms cannot occur fast enough to prevent the pressure under the indenter from exceeding the phase transformation threshold [39]. Upon unloading, different metastable phases may form (depending on the unloading rate and temperature), which will eventually transform back to the stable diamond cubic phase [25,40]. Figure 13 shows typical curves of the applied force plotted against penetration depth for the surfaces turned with the lowest (0.5 μm/rev) and highest (9 μm/rev) feedrates along the <11$\bar{2}$> cutting directions using a cube corner indenter. Compared to the Berkovich indentations performed at $P_{max} = 10$ mN (see Figs. 9(*a*) and 9(*b*)), the cube corner indenter resulted in larger maximum penetration depths during contact and larger permanent indentation depths after unloading. The cube corner indenter also produced larger pop-ins in the loading curves. During unloading the Berkovich indenter produced curves with the expected behavior of elastic recovery, while the cube corner indenter produced an elbow (marked by arrows). The elbow has been observed during indentation of single crystal Ge in cases where the β-Sn phase transforms to an amorphous phase upon unloading [24].

Figure 14 shows SEM images of the residual impressions of the cube corner indentations. An SEM image of the residual impression of a Berkovich indentation on the surface turned with a feedrate of 0.5 μm/rev is also shown for comparison. At all feedrates, material appeared to be extruded out of the contact area between the indenter and the surface. Similar observations have been reported during nanoindentation of single crystal diamond cubic Ge using a cube corner indenter, where the extruded material was attributed to the formation of a softer ductile phase (e.g., β-Sn) beneath the diamond indenter [25]. In contrast to the cube corner impressions, the impression of the Berkovich indentation exhibited no extruded material. These observations along with the observation of an elbow during unloading suggest that during indentation with a cube corner indenter, deformation is dominated by a phase transformation of Ge from a diamond cubic to a β-Sn phase [39], which upon unloading transforms to an amorphous phase [24].

As seen in Fig. 14, the length of the radial cracks observed in the post-indentation SEM images of the cube corner indentations decreased at higher feedrates. Crack propagation has been shown to cease when the driving force at the crack tip is in equilibrium with the material's fracture toughness [41]. Therefore, the smaller radial cracks observed at higher feedrates suggest an increase in the fracture toughness. The expression used to evaluate indentation fracture toughness (K_{IC}) from crack length ($2c$) depends on the crack morphology and indenter geometry. The following expression was adopted for radial cracks [42]:

$$K_{IC} = \alpha \sqrt{\frac{E}{H}} \frac{P_{max}}{c^{3/2}} \tag{5}$$

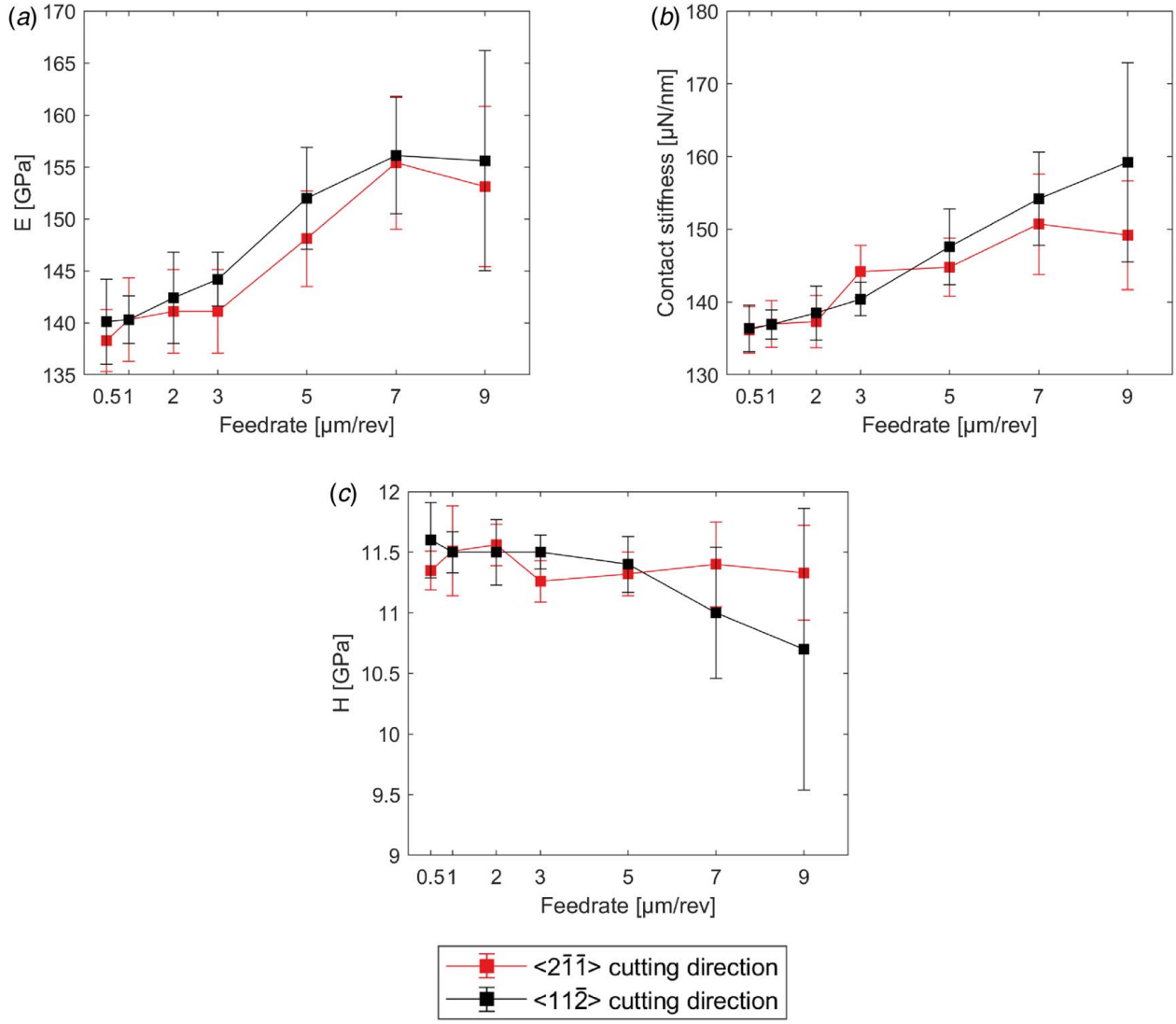

Fig. 12 Average and standard deviation of (*a*) elastic modulus, (*b*) contact stiffness, and (c) hardness of the (111)Ge surfaces turned with a range of feedrates along the <11$\bar{2}$> and <2$\bar{1}\bar{1}$> cutting directions

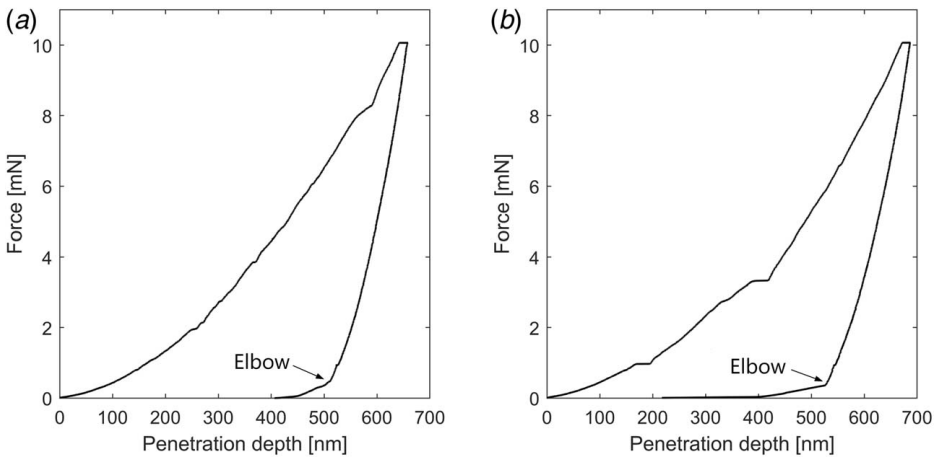

Fig. 13 Force applied to the cube corner indenter plotted against penetration depth for the surfaces turned with a feedrate of (*a*) 0.5 μm/rev and (*b*) 9 μm/rev along the <11$\bar{2}$> cutting directions

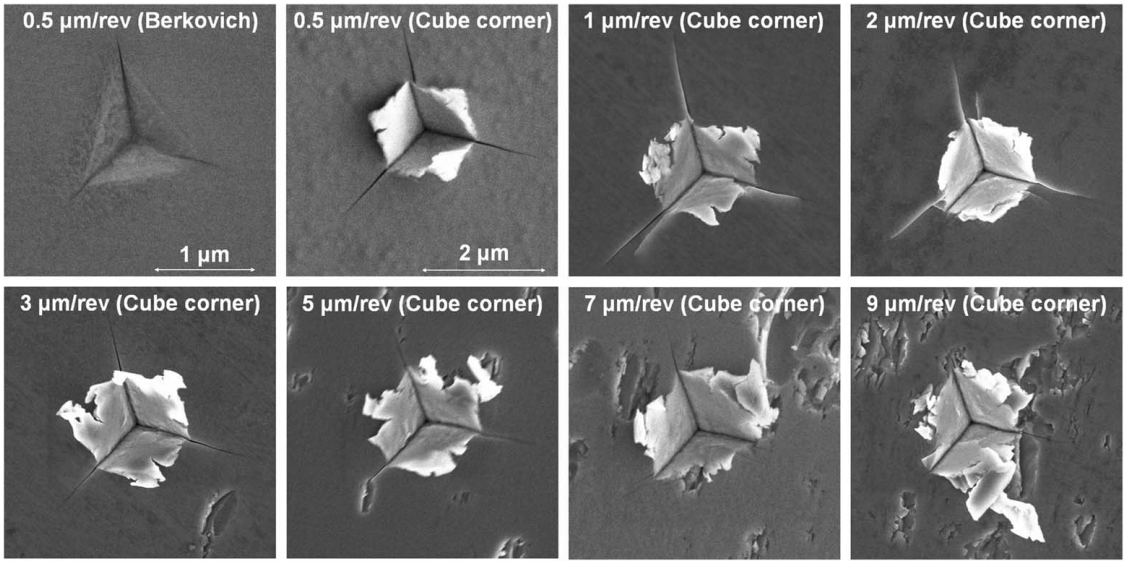

Fig. 14 Post-indentation SEM scans of the cube corner residual impressions on the surfaces turned along the <11$\bar{2}$> cutting directions. An SEM image of the residual impression from the Berkovich indentation on the surface turned with a feedrate of 0.5 μm/rev is also shown for comparison.

where α is the Lawn–Evans–Marshall constant (0.032 for a cube corner geometry [43]), and E and H are the elastic modulus and hardness of the turned surfaces obtained from the Berkovich indentations. Figure 15 shows the obtained values of K_{IC} for the surfaces turned with various feedrates. Each data point is the average of at least four indentations and the error bars represent ± 1 standard deviation. For the surfaces turned at $f < 3$ μm/rev, indentation fracture toughness was only minimally affected by feedrate. Increasing the feedrate to 3 μm/rev, which corresponded to the onset of brittle surface fracture, resulted in a ~23% increase in indentation fracture toughness. Further increase in feedrate led to a monotonic increase in indentation fracture toughness. The increase in near-surface compressive residual stress at higher feedrates that was characterized by Raman spectroscopy could have suppressed the propagation of radial cracks and is a plausible explanation for the observed increase in indentation fracture toughness [43].

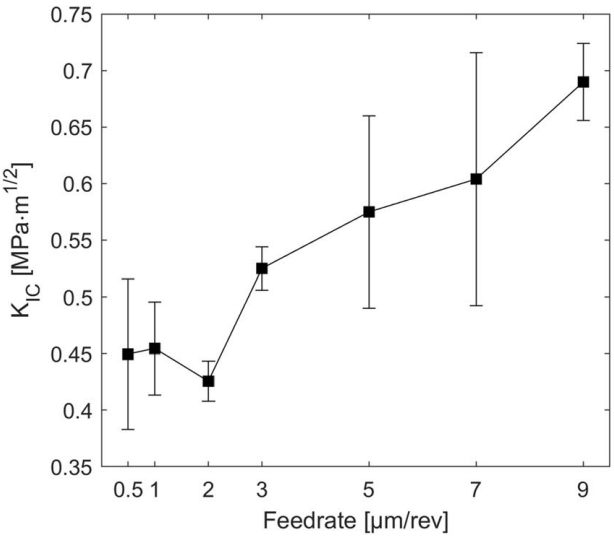

Fig. 15 Average and standard deviation of indentation fracture toughness of the (111)Ge surfaces turned with a range of feedrates along the <11$\bar{2}$> cutting directions

4 Conclusions

Increasing the feedrate (or a subsequent increase in maximum chip thickness) during the on-axis diamond turning of single crystal (111)Ge using a round nose tool resulted in a shift from indentation-dominant to cutting-dominant behavior. Characterization of the surface and subsurface damage demonstrated that at sufficiently low feedrates, brittle surface fracture is prevented. Compressive residual stress was found to be present at all feedrates and its magnitude significantly increased at higher feedrates. The <11$\bar{2}$> in-plane directions of (111)Ge showed a higher propensity for brittle fracture resulting in a higher surface roughness and a lower subsurface crystal quality, especially after transitioning to the brittle-dominated cutting domain.

Evaluation of the mechanical response of the turned surfaces using nanoindentation demonstrated that quasi-plastic deformation of (111)Ge can be accommodated through activation of various quasi-plasticity mechanisms including defect propagation, crack formation and extension, and phase transformation. The dominant quasi-plasticity mechanisms were found to be dictated by the geometry of the indenter which in turn affected the state of stress experienced by the material. Increasing the feedrate resulted in an increase in elastic modulus of the turned surfaces, plausibly due to the pinning of dislocations on machining-induced crystalline defects. Hardness, in contrast, was found to be insensitive to the feedrate and in-plane crystallographic orientations over a maximum indentation depth of 230–250 nm. The near-surface compressive residual stress suppressed the propagation of radial cracks and resulted in higher indentation fracture toughness values after the onset of brittle fracture.

Acknowledgment

This research was partially supported by the NSF I/UCRC Center for Freeform Optics (IIP-1338877 and IIP-1338898), NSF grants 1437225, 1437232, 2210365, and 2210394 and grants from the II-VI Foundation. The help of Mr. Matthew Luebbe with performing cube corner nanoindentation experiments and evaluation of indentation fracture toughness is gratefully acknowledged.

Conflict of Interest

There are no conflicts of interest.

Data Availability Statement

The datasets generated and supporting the findings of this article are obtainable from the corresponding author upon reasonable request.

References

[1] Patel, M., and Karamalidis, A. K., 2021, "Germanium: A Review of Its US Demand, Uses, Resources, Chemistry, and Separation Technologies," Sep. Purif. Technol., **275**, p. 118981.

[2] Kolesnikov, A. I., Kaplunov, I. A., and Smirnov, Y. M., 2005, "Optical Transparency of Crystalline Germanium," J. Opt. Technol., **72**(2), pp. 214–220.

[3] Dutterer, B. S., Lineberger, J. L., Smilie, P. J., Hildebrand, D. S., Harriman, T. A., Davies, M. A., Suleski, T. J., and Lucca, D. A., 2014, "Diamond Milling of an Alvarez Lens in Germanium," Precis. Eng., **38**(2), pp. 398–408.

[4] Owen, J. D., Troutman, J. R., Harriman, T. A., Zare, A., Wang, Y. Q., Lucca, D. A., and Davies, M. A., 2016, "The Mechanics of Milling of Germanium for IR Applications," CIRP Ann., **65**(1), pp. 109–112.

[5] Nakasuji, T., Kodera, S., Hara, S., Matsunaga, H., Ikawa, N., and Shimada, S., 1990, "Diamond Turning of Brittle Materials for Optical Components," CIRP Ann., **39**(1), pp. 89–92.

[6] Tunesi, M., Lucca, D. A., Davies, M. A., Zare, A., Gordon, M. C., Sizemore, N. E., and Wang, Y. Q., 2022, "Surface Integrity of Diamond Turned (100) Ge," CIRP Proc., **108**, pp. 665–669.

[7] Sparks, R. G., and Paesler, M. A., 1992, "Depth Profiling of Residual Stress Along Interrupted Test Cuts in Machined Germanium Crystals," J. Appl. Phys., **71**(2), pp. 891–897.

[8] Sparks, R. G., and Paesler, M. A., 1988, "Micro-Raman Analysis of Stress in Machined Silicon and Germanium," Precis. Eng., **10**(4), pp. 191–198.

[9] Shore, P., 1995, "Machining of Optical Surfaces in Brittle Materials Using an Ultra-Precision Machine Tool," Ph.D. dissertation, Cranfield University, Bedford, UK.

[10] Zhou, P., Yan, Y., Huang, N., Wang, Z., Kang, R., and Guo, D., 2017, "Residual Stress Distribution in Silicon Wafers Machined by Rotational Grinding," ASME J. Manuf. Sci. Eng., **139**(8), p. 081012.

[11] Guo, X., Li, Q., Liu, T., Kang, R., Jin, Z., and Guo, D., 2017, "Advances in Molecular Dynamics Simulation of Ultra-Precision Machining of Hard and Brittle Materials," Front. Mech. Eng., **12**(1), pp. 89–98.

[12] Momma, K., and Izumi, F., 2011, "VESTA 3 for Three-Dimensional Visualization of Crystal, Volumetric and Morphology Data," J. Appl. Crystallogr., **44**(6), pp. 1272–1276.

[13] Oliver, W. C., and Pharr, G. M., 1992, "An Improved Technique for Determining Hardness and Elastic Modulus Using Load and Displacement Sensing Indentation Experiments," J. Mater. Res., **7**(6), pp. 1564–1583.

[14] ISO 14577-2, 2015, "Metallic Materials—Instrumented Indentation Test for Hardness and Materials Parameters—Part 2: Verification and Calibration of Testing Machines."

[15] Higashi, H., Kasahara, K., Kudo, K., Okamoto, H., Moto, K., Park, J. H., Yamada, S., et al., 2015, "A Pseudo-Single-Crystalline Germanium Film for Flexible Electronics," Appl. Phys. Lett., **106**(4), p. 041902.

[16] Dutta, P., Rathi, M., Yao, Y., Gao, Y., Majkic, G., Iliev, M., Martinez, J., Holzapfel, B., and Selvamanickam, V., 2014, "Large Grained Single-Crystalline-Like Germanium Thin Film on Flexible Ni–W Tape," RSC Adv., **4**(40), pp. 21042–21048.

[17] Li, L., Fang, X., Chew, H. G., Zheng, F., Liew, T. H., Xu, X., Zhang, Y., Pan, S., Li, G., and Zhang, L., 2008, "Crystallinity-Controlled Germanium Nanowire Arrays: Potential Field Rmitters," Adv. Funct. Mater., **18**(7), pp. 1080–1088.

[18] Huang, X., Ninio, F., Brown, L. J., and Prawer, S., 1994, "Raman Scattering Studies of Surface Modification in 1.5 MeV Si-Implanted Silicon," J. Appl. Phys., **77**(11), pp. 5910–5915.

[19] Tiong, K. K., Amirtharaj, P. M., Pollak, F. H., and Aspnes, D. E., 1984, "Effects of As+ Ion Implantation on the Raman Spectra of GaAs: "Spatial Correlation" Interpretation," Appl. Phys. Lett., **44**(1), pp. 122–124.

[20] Dieter, G. E., 1989, *Mechanical Metallurgy*, McGraw-Hill Book Company, UK.

[21] Jacobus, K., DeVor, R. E., and Kapoor, S. G., 2000, "Machining-Induced Residual Stress: Experimentation and Modeling," ASME J. Manuf. Sci. Eng., **122**(1), pp. 20–31.

[22] Asaumi, K., and Minomura, S., 1978, "Effect of Pressure on the Raman Shift in Ge," J. Phys. Soc. Jpn., **45**(3), pp. 1061–1062.

[23] Olego, D., and Cardona, M., 1982, "Pressure Dependence of Raman Phonons of Ge and 3C-SiC," Phys. Rev. B, **25**(2), pp. 1151–1160.

[24] Huston, L. Q., Kiran, M. S. R. N., Smillie, L. A., Williams, J. S., and Bradby, J. E., 2017, "Cold Nanoindentation of Germanium," Appl. Phys. Lett., **111**(2), p. 021901.

[25] Jang, J. I., Lance, M. J., Wen, S., and Pharr, G. M., 2005, "Evidence for Nanoindentation-Induced Phase Transformations in Germanium," Appl. Phys. Lett., **86**(13), p. 131907.

[26] Bradby, J. E., Williams, J. S., Wong-Leung, J., Swain, M. V., and Munroe, P., 2002, "Nanoindentation-Induced Deformation of Ge," Appl. Phys. Lett., **80**(15), pp. 2651–2653.

[27] Oliver, D. J., Bradby, J. E., Williams, J. S., Swain, M. V., and Munroe, P., 2008, "Thickness-Dependent Phase Transformation in Nanoindented Germanium Thin Films," Nanotechnology, **19**(47), p. 475709.

[28] Oliver, D. J., Bradby, J. E., Williams, J. S., Swain, M. V., and Munroe, P., 2009, "Rate-Dependent Phase Transformations in Nanoindented Germanium," J. Appl. Phys., **105**(12), p. 126101.

[29] Lucca, D. A., Herrmann, K., and Klopfstein, M. J., 2010, "Nanoindentation: Measuring Methods and Applications," CIRP Ann.—Manuf. Technol., **59**(2), pp. 803–819.

[30] Tsui, T. Y., Oliver, W. C., and Pharr, G. M., 1996, "Influences of Stress on the Measurement of Mechanical Properties Using Nanoindentation: Part I. Experimental Studies in an Aluminum Alloy," J. Mater. Res., **11**(3), pp. 752–759.

[31] Bauer, C. L., and Gordon, R. B., 1962, "Mechanism for Dislocation Pinning in the Alkali Halides," J. Appl. Phys., **33**(2), pp. 672–682.

[32] Dieckamp, H., and Sosin, A., 1956, "Effect of Electron Irradiation on Young's Modulus," J. Appl. Phys., **27**(12), pp. 1416–1418.

[33] Oliver, D. J., Ruffell, S., Bradby, J. E., Williams, J. S., Swain, M. V., Munroe, P., and Simpson, P. J., 2009, "Nanoindentation of Ion-Implanted Crystalline Germanium," Phys. Rev. B—Condens. Matter Mater. Phys., **80**(11), p. 115210.

[34] Novak, M., Lofaj, F., and Hviscova, P., 2013, "The Effect of Residual Stresses on Nanoindentation Behavior of Thin W-C Based Coatings," Powder Metall. Prog., **13**(3–4), pp. 132–138.

[35] Zare, A., Su, Q., Gigax, J., Shojaee, S. A., Nastasi, M., Shao, L., and Lucca, D. A., 2017, "Effects of Ion Irradiation on Structural and Mechanical Properties of Crystalline Fe/Amorphous SiOC Nanolaminates," Acta Mater., **140**, pp. 10–19.

[36] Fischer-Cripps, A. C., 2011, *Nanoindentation, Vol. 2*, Springer, New York.

[37] Pharr, G. M., Tsui, T. Y., Bolshakov, A., and Oliver, W. C., 1994, "Effects of Residual Stress on the Measurement of Hardness and Elastic Modulus Using Nanoindentation," MRS Online Proc. Libr., **338**, pp. 127–134.

[38] Jang, J. I., and Pharr, G. M., 2008, "Influence of Indenter Angle on Cracking in Si and Ge During Nanoindentation," Acta Mater., **56**(16), pp. 4458–4469.

[39] Roundy, D., and Cohen, M. L., 2001, "Ideal Strength of Diamond, Si, and Ge," Phys. Rev. B, **64**(21), p. 212103.

[40] Kiran, M. S. R. N., Haberl, B., Bradby, J. E., and Williams, J. S., 2015, *Semiconductors Semimetals,* Vol. 91, Elsevier, New York. pp. 165–203.

[41] Casellas, D., Caro, J., Molas, S., Prado, J. M., Valls, I., 2007, "Fracture Toughness of Carbides in Tool Steels Evaluated by Nanoindentation," Acta Mater., **55**(13), pp. 4277–4286.

[42] Anstis, G. R., Chantikul, P., Lawn, B. R., and Marshall, D. B., 1981, "A Critical Evaluation of Indentation Techniques for Measuring Facture Toughness: I, Direct Crack Measurements," J. Am. Ceram. Soc., **64**(9), pp. 533–538.

[43] Lugovy, M., Slyunyayev, V., Orlovskaya, N., Blugan, G., Kuebler, J., and Lewis, M., 2005, "Apparent Fracture Toughness of Si_3N_4-Based Laminates With Residual Compressive or Tensile Stresses in Surface Layers," Acta Mater., **53**(2), pp. 289–296.